

Mechanical model of the left ventricle of the heart approximated by axisymmetric geometry

F. A. Syomin* and A. K. Tsaturyan*

Abstract — An axisymmetric model is suggested to simulate mechanical performance of the left ventricle of the heart. Cardiac muscle is treated as incompressible anisotropic material with active tension directed along muscle fibres. This tension depends on kinetic variables that characterize interaction of contractile proteins and regulation of muscle contraction by calcium ions. For numerical simulation of heartbeats the finite element method was implemented. The model reproduces well changes in ventricle geometry between systole and diastole, ejection fraction, pulse wave of ventricular and arterial pressure typical for normal human heart. The model also reproduces well the dependence of the stroke volume on end-diastolic and arterial pressures (the Frank–Starling law of the heart and Anrep effect). The results demonstrate that our model of cardiac muscle can be successfully applied to multiscale 3D simulation of the heart.

Keywords: Heart, cardiac muscle, muscle contraction, mathematical model, finite elements.

MSC 2010: 74L15, 92C10, 92C30, 74S05

Computer modelling of the heart mechanics is a fast developing field of computational physiology. During the last two decades a number of electromechanical models of the whole heart or its left ventricle has been developed [26]. Such multiscale models usually combine several models that describe electrical and chemical processes at the level of a single cell with mechanical properties of cardiac muscle tissue. Generally, a model of the heart consists of a model of ionic currents in the cardiomyocytes, model of myocardial mechanics, model of blood circulation (haemodynamics model), and a geometrical approximation of the heart. In spite of the presence of 3D models with patient-specific geometry of hearts and very detailed description of ionic currents, those models do not provide accurate description of cardiac muscle mechanics. The problem is that fine detailed models of actin-myosin interaction that underlies development of active stress in cardiac muscle are specified by systems of partial differential equations, and thus they are too complicated for numerical simulation. On the other hand, prevailed simple models that are set by the systems of a few ODEs do not reproduce some major properties of cardiac muscle.

To overcome the problem stated above, we have developed a mechanical model of myocardium specified by a system of ODEs. The model is based on a kinetic

*Institute of mechanics MSU, Mitchurinsky prosp. 1, Moscow 119192, Russia. E-mail: tsat@imec.msu.ru, ted.syomin@yandex.ru

The work was supported by the RFBR (grants 15-04-02174 and 16-04-00693).

model of muscle contraction and its regulation [21, 22]. The model reproduces a series of different uniaxial experiments performed on striated muscles. Some of them are steady-state shortening and lengthening at full activation, steady-state force-calcium dependencies, responses of force or length to step-like changes in muscle length or load, isometric and isotonic contractions at full activation and with consideration of regulation processes. Later we have applied this model to the simulation of contraction of the left ventricle approximated by a thick-walled cylinder [23], describing blood circulation by a simple compartmental model (Windkessel model). This approbation of the model has shown satisfactory results. We were able to reproduce the time course of the major haemodynamical and geometrical values during a heartbeat of an average 'healthy' heart and under conditions that are typical for hypertrophic and dilated cardiomyopathies. After improving our circulation model, we have also investigated numerically the dependence of ventricular performance (ejection fraction of the ventricle) on the ventricle preload (end-diastolic pressure) and afterload (peripheral resistance or arterial pressure) [24]. The simulation reproduces the Frank–Starling law of the heart, pressure-volume loops, and the Anrep effect.

At the next step of 3D modelling of the heart with patient-specific geometry we approximated the ventricle shape by a thick-walled body of revolution more similar to real heart than a cylinder. Here we describe a finite element model of pumping function of the ventricle based on our model of cardiac muscle.

1. Statement of the problem

1.1. Material and geometry

We approximated the ventricle by a thick-walled body of revolution with the shape close to semi-ellipsoid. To set up the geometry we used curvilinear coordinate system (γ, ψ) introduced in [17]. Here γ corresponds to the position of a point in the wall of the ventricle: $\gamma = 0$ for inner points of the ventricle (subendocardium), and $\gamma = 1$ for outer points of the ventricle (subepicardium). Coordinate ψ corresponds to the position of the point between base ($\psi = 0$) and apex ($\psi = \pi/2$) of the ventricle. These coordinates can be expressed in terms of cylindrical coordinates as follows

$$\begin{aligned} r &= (r_{\text{in}} + \gamma(r_{\text{out}} - r_{\text{in}}))(\varepsilon \cos \psi + (1 - \varepsilon)(1 - \sin \psi)) \\ z &= (h_{\text{in}} + \gamma(h_{\text{out}} - h_{\text{in}}))(1 - \sin \psi) + (1 - \gamma)(h_{\text{out}} - h_{\text{in}}) \end{aligned} \quad (1.1)$$

where r_{in} and r_{out} are the inner and outer radii at $\psi = 0$, h_{in} and h_{out} are the lengths of the ventricle axis between the ventricular base and the inner and outer axial point, respectively. Parameter ε sets the curvature of the ventricle. The shape is conic for $\varepsilon = 0$, and when $\varepsilon = 1$ the shape is a body of revolution with ψ being inclination angle of a point. We have chosen $\varepsilon > 1$ in order to approximate the region of tapering from the widest part of the ventricle to its region of fibrous valve.

The myocardium was considered to be hyperelastic incompressible transversely-isotropic medium with active stress caused by mechanochemical processes. The

constitutive equation in its general form looks like

$$\mathbf{T} = \mathbf{T}_{is} - p\mathbf{E} + \left(\frac{F_{act} + F_{tit}}{L_s/L_{s0}} \right) \cdot \mathbf{B}. \quad (1.2)$$

Here L_{s0} is a length of unstrained sarcomere, L_s is a length of deformed sarcomere, \mathbf{T} is Cauchy stress tensor, \mathbf{T}_{is} is an isotropic part of passive stress tensor, p is a Lagrange multiplier, or pressure, \mathbf{E} is a unit tensor, \mathbf{B} is a tensor of fibres orientation, which is equal to dyadic product of deformed unit vectors aligned with muscle fibres. The scalar F_{act} is active tension of cardiac muscle, and F_{tit} is a component of passive tension caused by non-linearly elastic titin fibres. Both tensions are caused by the forces aligned with fibres and applied at the cross-section of a fibre. Passive stress of hyperelastic material was expressed using strain energy function W , which depends on the first and second invariants I_1 and I_2 of the right Cauchy–Green deformation tensor \mathbf{G} :

$$\begin{aligned} \mathbf{T}_{is}^{ij} &= \frac{\partial W}{\partial \varepsilon_{ij}} \\ W &= c_{is}^1 e^{Q(I_1, I_2)} \\ Q &= c_{is}^2 \cdot \left(0.25(I_1 - 3)^2 - 0.5(I_2 - 2I_1 + 3) \right). \end{aligned} \quad (1.3)$$

Here ε_{ij} are the components of the Gauchy–Green strain tensor, c_{is}^1 and c_{is}^2 are the material parameters. The strain energy function was based on that suggested in [5]. The general forms of expressions for the first and the second invariants are as follows:

$$I_1(\mathbf{G}) = \mathbf{E} \bullet \bullet \mathbf{G} = \sum_i G_i^i, \quad I_2(\mathbf{G}) = (I_1^2(\mathbf{G}) - I_1(\mathbf{G}^2)) / 2$$

where ‘ $\bullet \bullet$ ’ is a notation for double tensor contraction. Titin force F_{tit} was specified by so-called worm-like chain model [13], which is often used for description of stresses in long molecular chains, and was set by equation

$$F_{tit} = \frac{6k_B T \rho_m}{L_p} \cdot \left(\frac{0.25}{(1 - 0.5 \cdot (L_s - L_{s0})/L_c)^2} - 0.25 + \frac{0.5 \cdot (L_s - L_{s0})}{L_c} \right). \quad (1.4)$$

Here L_c is a contour length of titin, L_p is a persistent length of titin, ρ_m is a number of myosin filaments per unit of cross-section area of unstrained muscle, k_B is a Boltzmann constant, and T is an absolute temperature.

Active force F_{act} is defined by a kinetic model of cardiac muscle [21, 22] based on the following concept. Muscle contraction is caused by relative sliding of two sets of protein filaments in an elementary contractile unit of muscle—sarcomere. These filaments are thick myosin filament and thin actin filament. Myosin heads protruding from the backbone of thick filaments are molecular motors, which produce force during their interaction with actin molecules. During contraction these

myosin heads go through Lymn–Taylor cycle. According to the cycle a myosin head can be in detached from actin state (state 0), or it can attach to actin and form a cross-bridge. A cross-bridge can attach actin weakly (state 1), or strongly (state 2). In the latter case, it generates active force and/or causes displacement. Our model of contraction is based on the Lymn–Taylor cycle and considers muscle activation as well. In the absence of calcium ions, Ca^{2+} , a complex of regulatory proteins covers myosin binding sites on actin and causes muscle relaxation. The binding of Ca^{2+} to regulatory protein troponin-C and formation of CaTnC (calcium-troponin C) complex suspends the inhibition and opens actin filaments for myosin binding. The formation and dissociation of the CaTnC complexes depends on a number of factors. The affinity of the complexes to Ca^{2+} ions increases with an increase in sarcomere length (length-dependent activation), a number of already formed CaTnC complexes, and a number of strongly bound cross-bridges [4]. These cooperative effects are also taken into consideration in our model. Main variables of our contraction model are:

1. n is a probability of a myosin head to be attached to thin filament.
2. ϑ is a fraction of strongly bound cross-bridges.
3. δ is an ensemble-averaged distortion of cross-bridges.
4. L_s is a sarcomere length.
5. A_1 is a probability of formation of a CaTnC complex in the zone of overlap of thick and thin filaments where cross-bridges can be formed.
6. A_2 is a probability of formation of a CaTnC complex outside the overlap zone.
7. C_{Ca} is a concentration of free intracellular calcium ions.

The system of ODEs for our contraction model is as follows

$$\begin{aligned}
\frac{\partial n}{\partial t} &= k_{01}(\delta) \cdot (A_1 - n) - k_{10}(\delta) n \cdot (1 - \vartheta) - k_{20}(\delta) n \vartheta \\
\frac{\partial (n\vartheta)}{\partial t} &= k_{12}(\delta) n \cdot (1 - \vartheta) - k_{21}(\delta) n \vartheta - k_{20}(\delta) n \vartheta \\
\frac{\partial \delta}{\partial t} &= \dot{L}_s - \frac{k_{01}(\delta) \cdot (1 - n)}{n} \delta \\
\frac{\partial A_1}{\partial t} &= \begin{cases} \alpha_{01}(C_{Ca})(1 - A_1) - \alpha_{101}(L_s, n\vartheta, A_1)A_1, & \frac{\partial W_{ovA}}{\partial t} \leq 0 \\ \alpha_{01}(C_{Ca})(1 - A_1) - \alpha_{101}(L_s, n\vartheta, A_1)A_1 + \frac{\partial W_{ovA}}{\partial t} \cdot \frac{A_2 - A_1}{W_{ovA}}, & \frac{\partial W_{ovA}}{\partial t} > 0 \end{cases} \\
\frac{\partial A_2}{\partial t} &= \begin{cases} \alpha_{01}(C_{Ca})(1 - A_2) - \alpha_{102}(L_s, A_2)A_2 - \frac{\partial W_{ovA}}{\partial t} \cdot \frac{A_1 - A_2}{1 - W_{ovA}}, & \frac{\partial W_{ovA}}{\partial t} \leq 0 \\ \alpha_{01}(C_{Ca})(1 - A_2) - \alpha_{102}(L_s, A_2)A_2, & \frac{\partial W_{ovA}}{\partial t} > 0 \end{cases} \\
\frac{\partial C_{Ca}}{\partial t} &= I_{Ca}(t) - Y_{Ca}(C_{Ca} - C_{Ca}^*) - C_{Tn} \cdot \frac{\partial (A_1 W_{ovA} + A_2 (1 - W_{ovA}))}{\partial t}.
\end{aligned} \tag{1.5}$$

The transitions between weakly and strongly bound states are much more faster than other transitions. Therefore we excluded the second equation from (1.5) and expressed ϑ from steady-state solution as function of δ

$$\vartheta(\delta) = \frac{k_{12}(\delta)}{k_{12}(\delta) + k_{21}(\delta) + k_{20}(\delta)}$$

and active tension was set by expression

$$F_{\text{act}} = E_{cb} N_{cb} \rho_m W_{ov} n(\delta + \vartheta h). \quad (1.6)$$

In equations (1.5) and (1.6) k_{ij} are the rates of transitions of a myosin head from state i to state j , α are the rates of CaTnC formation and dissociation, W_{ov} and W_{ovA} are the normalized in different ways lengths of overlapping zone, E_{cb} is a cross-bridge stiffness, N_{cb} is the number of myosin heads per half of a sarcomere, h is a cross-bridge strain during its transition to strongly bound state in the absence of load, I_{Ca} is a time-function of calcium inflow, Y_{Ca} is a calcium uptake constant, C_{Ca}^* is a small constant, and C_{Tn} is the total concentration of regulatory complexes.

Further we took into account some regional features of the ventricle. Firstly, the region of fibrous ring of the ventricle (basal region) is much more stiff than the rest of it because of circumferential fibres of collagen that are prevalent in the region [8]. This ‘fibrous skeleton’ is mostly concentrated in the inner part of the ventricle, where the valves and their leaflets are located. Therefore we added a tensor \mathbf{T}_b of anisotropic passive stress. In order to describe the continuous variation in stiffness caused by density of circumferential collagen fibres from equator (region with maximal radius according to (1.1)) to base and from subepicardium to subendocardium we increased passive stiffness of myocardium respectively by a power function with exponent p_b . Secondly, we supposed, as it was confirmed by experimental data, that fibres of cardiac muscle in the most part of the ventricle are oriented along spirals with angle to the base plane changing smoothly from 80° at subendocardium to -55° at subepicardium [20]. However, in the apical region a number of muscle fibres seem to be oriented randomly due to widely distributed transmural orientation of the fibres and due to asymmetry of orientation distribution at the apex [7, 25]. To describe this feature we considered additional isotropic Hookian-elastic stress with stiffness coefficient depending on a number of cross-bridges as stiffness of activated muscle is proportional to the fraction of actin-bound cross-bridges. This term increased continuously from equator to apex as a power function with exponent p_{ap} and multiplier c_{ap} .

The final form of constitutive equation is

$$\begin{aligned}
\mathbf{T} &= \mathbf{T}_{is} + \mathbf{T}_b - p\mathbf{E} + \left(\frac{F_{\text{act}} + F_{\text{tit}}}{L_s/L_{s0}} \right) \cdot \mathbf{B} \\
\mathbf{T}_{is}^{ij} &= \begin{cases} \frac{\partial W}{\partial \varepsilon_{ij}}, & \psi \leq \psi_0 \\ \frac{\partial W}{\partial \varepsilon_{ij}} + c_{ap} F_{\text{act}}^0 \left(\frac{\psi - \psi_0}{\pi/2 - \psi_0} \right)^{p_{ap}} \varepsilon_{ij}, & \psi > \psi_0 \end{cases} \\
F_{\text{act}}^0 &= E_{cb} N_{cb} \rho_m n h \vartheta(0) \\
\mathbf{T}_b^{\varphi\varphi} &= \begin{cases} c_b \left(\frac{\psi_0 - \psi}{\psi_0} \right)^{p_b} (1 - \gamma)^{p_b} \left(\frac{1}{r} \right)^2 \left(1 - \frac{1}{\sqrt{L_s/L_{s0}}} \right), & \psi \leq \psi_0 \\ 0, & \psi > \psi_0 \end{cases} \\
\mathbf{T}_b^{ij} &= 0, \quad i \neq \varphi, \quad j \neq \varphi.
\end{aligned} \tag{1.7}$$

Here r is a radial coordinate, and ψ_0 is a value of coordinate ψ at which maximal value of inner radius of unstrained ventricle is reached.

1.2. Finite elements model

We set a mixed problem for node displacements and pressure values that result from incompressibility. It is known that the use of simplex triangle elements with linear approximation causes troublesome effects for fully incompressible materials such as volumetric and shear locking. In order to avoid these problems, but still use simplex triangles we connected triangles by pairs and wrote down incompressibility equations for rings formed by rotation of each quadrilateral element. Unknown pressures were also determined per quadrilateral. Model equations were based on the equations of energy balance. For an element the equation takes form of

$$\int_{V_e} \tilde{\mathbf{T}}^{ij} \hat{\varepsilon}_{ij} dV = \mathbf{p}_{e,m} \hat{\mathbf{u}}_e^m \tag{1.8}$$

where V_e is a volume of unstrained element, $\tilde{\mathbf{T}}$ is the second Piola-Kirchhoff stress tensor, $\mathbf{p}_{e,m}$ is a vector of force applied at the node denoted by number m in local numeration of element e , $\hat{\mathbf{u}}_e^m$ is a vector of displacement for the same node. The equations were written down in cylindrical coordinates. To get the global form of the equations for a node we summed the left and right hand sides of the equations over elements adjacent to this node. As it was stated earlier, we also wrote down the following incompressibility equations for each pair of triangular rings e_1 and e_2

$$\frac{d}{dt} \left(\int_{V_{e_1}} dV + \int_{V_{e_2}} dV \right) = 0 \Rightarrow r_{e_1} S_{e_1}^0 + r_{e_2} S_{e_2}^0 = R_{e_1} S_{e_1}^1 + R_{e_2} S_{e_2}^1 \tag{1.9}$$

where r_{e_i} and R_{e_i} are the reference and deformed radial coordinates of centre points of triangle elements in fixed coordinate system, and $S_{e_i}^j$ are the areas of deformed ($j = 1$) and undeformed ($j = 0$) triangles.

The equations were rewritten in form of small increments, i.e., we linearized the equations for small increments of displacements, forces, and pressures. We calculated integrals over elements by the Gaussian quadrature method with three integration points per triangle. At each time step we were solving the system of linear equations for increments of displacements and pressure values. They were $3N_n$ energy balance equations for nodes, $N_e/2$ incompressibility equations (1.9) and an equation for ventricular volume. Here we denoted the total node number and element number by N_n and N_e , respectively. In addition, at each time step we were searching for unknown variables of the kinetic model at every integration point, and therefore we were solving $3N_e$ systems (1.5) of ODEs of the kinetic model by the explicit Euler method. After computation of all model variables at integration points we used method of superconvergent patch recovery [9] to find node values of the variables for output.

The ventricle model was completed by haemodynamics model that is described in detail in [24] and was originally based on compartment model [2]. The model considers only systemic blood circulation, and pressure in the left atrium is set to venous pressure.

1.3. Boundary and initial conditions

At base of the ventricle nodal axial and angular displacements were fixed to avoid rigid body motion. Instead of these displacements nodal forces were set as unknown variables. External forces at inner nodes of the ventricle were equal to forces of ventricular blood pressure. Pressure on outer surface of ventricular wall was set to zero. Initial conditions of haemodynamics model were set to provide normal volume of blood in systemic circulation, their values are the same as those presented in [24]. To avoid difficulties with zero initial conditions for the kinetic model (n is in denominator in equation for δ in (1.5)) we set n , A_1 and C_{Ca} to the values of steady-state solution at $\delta = 0$.

Expressions (1.1) for ventricular geometry are not appropriate for early diastolic geometry, that is usually considered as unloaded configuration. They can not fit well the taper region located above wide equatorial region up to fibrous ring. Therefore we used (1.1) to set the end-systolic geometry, which was preliminarily considered to be unloaded configuration. At that state sarcomeres had minimal length of $1.7 \mu\text{m}$, which was set as preliminary unstrained sarcomere length L_{s0} . The geometrical parameters of (1.1) were chosen in order to fit experimental values of the end-systolic ventricular dimensions and wall thickness. Then we were filling the ventricle to the volume of 120 ml and were varying elastic parameter c_{is}^1 until ventricular pressure was equal to 5 mm Hg at 120 ml volume. The second parameter of strain energy function, c_{is}^2 , was chosen on the basis of expression for strain energy function from [11] and was fixed. It is known that sarcomeres in passive

relaxed muscle have lengths of approximately $1.9 \mu\text{m}$ [16]. Streeter has shown in his review [19] that sarcomere lengths in early diastole equal $1.9 \mu\text{m}$ throughout ventricular wall. Taking into account these facts we chose ventricular geometry at the moment when the major part of sarcomeres had lengths near $1.9 \mu\text{m}$ and set it as the final reference unloaded state. Due to a small difference in titin passive stress at sarcomere lengths of 1.7 and $1.9 \mu\text{m}$ we were able to reset unstrained sarcomere length $L_{s0} = 1.9 \mu\text{m}$. Thereafter we adjusted c_{is}^1 again to obtain the end-diastolic pressure and volume of 5 mm Hg and 120 ml , respectively. Final value of c_{is}^1 matched its value from [11] very well while end-diastolic ventricular dimensions [12] and thickness of ventricular walls at various regions of the ventricle [10] were in good agreement with experimental data.

The rates of kinetic processes in our model of cardiac muscle contain a number of parameters. The rates and values of the parameters were specified previously [21, 22]. The parameters of blood circulation and their values are presented in [23, 24] The values of all parameters that are mentioned in this article are presented in Table 3.

2. Results and discussion

In order to test our implementation of finite element method we used it for solving Lamé problems of thick-walled cylinder and sphere under inner pressure. These bodies were considered to be made of isotropic hyperelastic material with strain energy function (1.3). We have obtained quite accurate results that closely fitted to the analytical solution. The next test problem we set was the problem of contraction of the left ventricle approximated by a cylinder. All model parameters were the same as in [23]. Since we did not consider electrical activation, we just set influx of calcium ions to a muscle cell as a periodic function of time based on $I_{Ca}(t)$ function for a single twitch contraction. Such activation was simultaneous for all elements. The simulation was running until we got periodical solution with a prescribed accuracy. Results of the simulation, namely the time-course of haemodynamic variables, inner radial and axial deformation, and twist angle, were very close to the numerical solution of one-dimensional problem obtained in [23].

Further we have simulated the contraction of normal human ventricle with geometrical approximation (1.1). Time step was set equal to 0.1 ms . All results that are shown below were computed with a mesh of 720 elements. The mesh had 11 nodes (20 triangular elements) throughout ventricular wall (γ coordinate) and 37 nodes along ψ coordinate. The computation of stiffness matrix was parallelized using OpenMP API, and it took ≈ 45 minutes to simulate one second of heart-beat with

Table 1. Relative errors of peak values of ventricular pressure (P_{LV}) and ventricular volume (V_{LV}) at the different time and space mesh steps.

Mesh	$\times 2$ time step	$\times 2\gamma$	$\times 2\psi$	$\times 0.5\gamma$	$\times 0.5\psi$
P_{LV}	0.00022	0.00033	0.00015	0.00135	0.00091
V_{LV}	0.0013	0.00017	0.00035	0.00043	0.0021

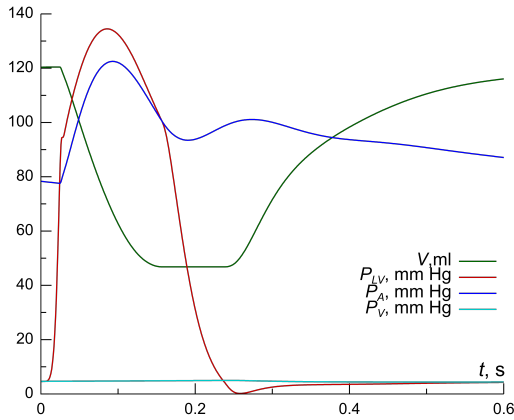


Figure 1. Computed haemodynamic variables during a heart-beat simulation. The time-courses of ventricular pressure (red, mm Hg), aortic pressure (blue, mm Hg), venous pressure (cyan, mm Hg), and ventricular volume (green, ml) are presented. Horizontal axis is for time in seconds.

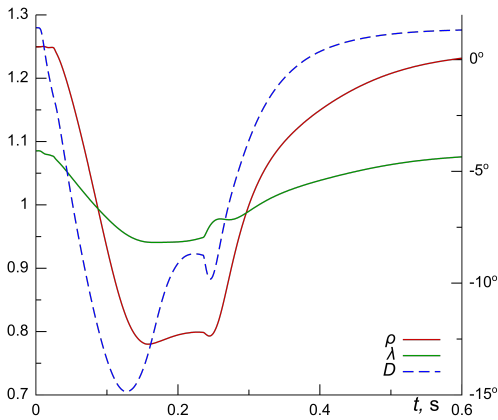


Figure 2. Time-course of geometric representative values during a heart-beat simulation. The left vertical axis is for changes in normalized short axis ρ (red, solid line) and long axis λ (green, solid line) dimensions. The right one is for time-course of typical twist angle D (blue, dashed line). Horizontal axis is for time in seconds.

a 24 core workstation. Further we compared resulting typical values of haemodynamical variables computed at various mesh sizes. The upper limit of a time step was ≈ 0.125 ms because of the 'fast' terms in equations (1.5) for the formation of CaTnC complexes (equations for A_1 and A_2), so we did not consider lesser step sizes than the default one. Table 1 contains relative errors for peak ventricular pressure and volume obtained with different mesh size.

Figure 1 shows time-course of haemodynamic variables of the model during a heart-beat. The results are in a good qualitative accordance with experimental data. There is also quantitative match of the computed results and experimental data for the representative values of pressures and volume that can be measured in humans. Namely, those are the end-systolic, end-diastolic, maximal, and minimal values.

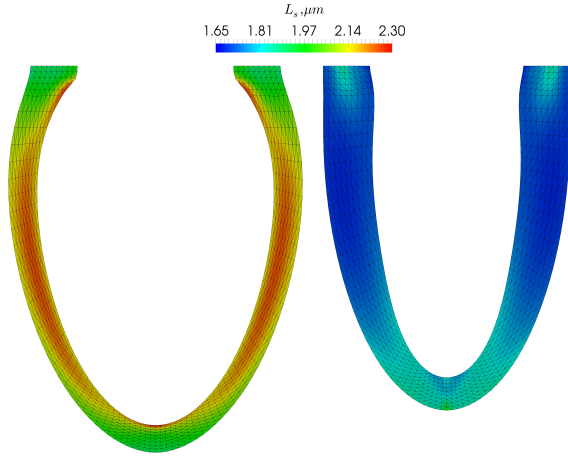


Figure 3. Map of sarcomere lengths at end-diastole (right) and end-systole (left).

Table 2. Transmural radial strain distribution (end-systolic with respect to end-diastolic).

region	endo	epi
basal	49%	33%
apical	31%	18%

Table 3. Parameter values.

r_{in}	1.73 cm	c_{is}^1	5.5 kdyn/cm ²
r_{out}	2.78 cm	c_{is}^2	3
h_{in}	6.93 cm	ρ_m	$1.42 \cdot 10^{-3} \text{ nm}^{-2}$
h_{out}	7.68 cm	L_c	0.35 μm
ε	1.1	L_p	8.38 nm
c_b	10^3 kdyn/cm^2	N_{cb}	150
c_{ap}	1.25	E_{cb}	1.75 pN/nm
p_b	5	$k_B T$	4 pH · nm
p_{ap}	5	C_{Tn}	30 μM
h	10 nm	C_{Ca}^*	0.01 μM
L_{s0}	1.9 μm	Y_{Ca}	4500 $\mu\text{M/s}$

The value of ventricular ejection fraction (the fraction of the end-diastolic volume of blood that was ejected into aorta per systole) equals approximately 62%, that is also in the range of values measured for healthy human hearts [3]. Figure 2 shows changes in the ventricle geometry during a heart-beat. We denoted the relative radial strain of the inner node that is the most distant from the axis at diastole by $\rho = R_{\max}/r_{\max}$, where r_{\max} and R_{\max} are the radial coordinate of that node in undeformed and deformed state, respectively. We denoted the relative axial strain of the inner axial node of the ventricle apex by $\lambda = H_{\max}/h_{\max}$. Here H_{\max} and h_{\max}

are the inner length of the ventricle in deformed and undeformed state, respectively; $D = \arctan(u^\theta r / (r + u^r))$ is for the twist of one of the outer nodes in the middle of apex region (at axial distance of ≈ 1.5 cm from apex); u^r and u^θ are the radial and angular displacements of the node, and r is its radial coordinate in undeformed state. Since the angular displacements of the basal nodes of the model ventricle were fixed, one can consider D as the ventricular twist angle and compare it with experimental full twist (apex rotation + basal rotation). Again end-systolic, end-diastolic, maximal, and minimal values, as well as the changes in thickness of ventricular wall are in agreement with clinical data [10, 12, 18]. New geometrical approximation also allowed us to compare local strains in the different regions of ventricular wall with experimental data. Longitudinal strains in basal region, mid-wall and apical regions were approximately equal to 21%, 17%, and 13%, respectively. We should notice that ‘basal’ region in experiments is quite far away from stiff fibrous ring and considered to be located near equatorial region of our simulated ventricle. These values are close to experimental values measured in human hearts [1]. Transmural distribution of longitudinal strain in ‘basal’ region was compared with data from [27]. Strain values were equal to 16% at subendocardium and 14% at subepicardium. We also calculated radial strains at subendo- and subepicardium in the different regions of the ventricle. The values are shown in Table 2. The results are in good agreement with data from [27]. Figure 3 shows the ventricle geometry and a map of distribution of sarcomere length over ventricular wall at end-systole and end-diastole. Taking into account that sarcomere lengths in unloaded ventricle equal $1.9 \mu\text{m}$ one can estimate local relative fibre strains.

To examine performance of the model ventricle and influence of length-dependent activation and cooperative effects in our muscle model on pumping function of the ventricle we simulated ventricle contraction at various preload and afterload. The dependences of major haemodynamic variables are presented in Fig. 4. The results show an increase of stroke volume with the increase in preload, which validate the Frank–Starling law for the model. For typical experimental curves one can see [15]. We also plotted pressure-volume diagrams (pressure-volume loops), which are often analyzed in medical practice. The loops are shown in Fig. 5. ESPVR (end-systolic pressure-volume relationship) line, which connects end-systolic points of pressure-volume loops, has a high slope typical for the Frank–Starling law. Similar pressure-volume loops for pig hearts can be found, e.g., in [6]. Figure 6 shows dependences of haemodynamic variables on peripheral resistance, which characterizes afterload. One can see that ejection volume slowly decreases with threefold increase in peripheral resistance while ventricular and aortic pressures increase drastically. The results are evidence of compensation process called the Anrep effect. Tables with experimental data can be found in [14].

3. Conclusion

We have performed numerical simulation of contraction of the left ventricle approximated by axisymmetric body, while material of the ventricle, myocardium,

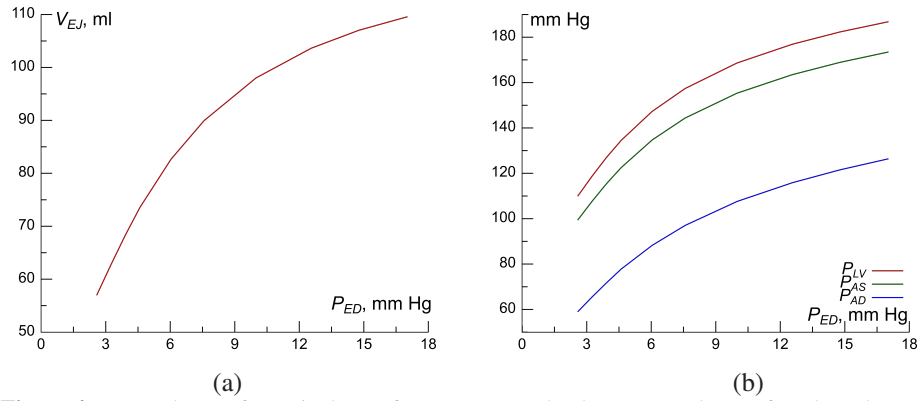


Figure 4. Dependence of ventricular performance on preload. (a) Dependence of stroke volume (V_{EJ}) on end-diastolic pressure (P_{ED}). (b) Dependence of ventricular pressure (P_{LV}), maximal systolic aortic pressure (P_{AS}) and minimal diastolic aortic pressure (P_{AD}) on end-diastolic pressure (P_{ED}).

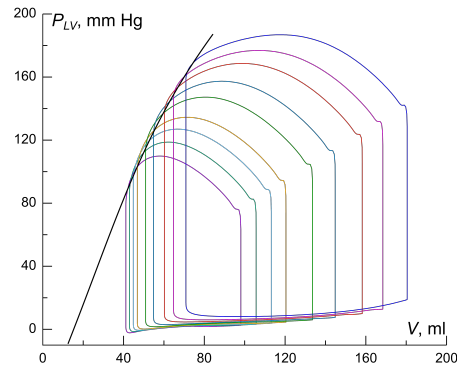


Figure 5. Pressure-volume diagrams at the different preload values.

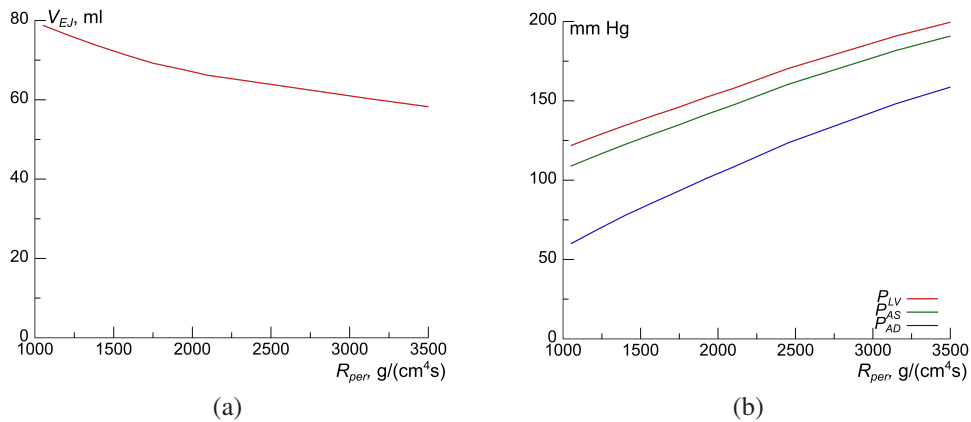


Figure 6. Dependence of ventricular performance on afterload. (a) Dependence of stroke volume (V_{EJ}) on peripheral resistance (R_{per}). (b) Dependence of ventricular pressure (P_{LV}), maximal systolic aortic pressure (P_{AS}) and minimal diastolic aortic pressure (P_{AD}) on peripheral resistance (R_{per}).

was modelled by quite accurate mechanical model with low computational cost. Suggested model reproduces features of ventricular geometry and blood circulation during heart-beat under various haemodynamic conditions including local geometrical changes. The results of simulation are promising and encourage us to use our myocardium model for more complex problems like 3D modelling of heart with patient-specific geometry.

References

1. A. Baltabaeva, M. Marciniak, B. Bijmens, J. Moggridge, F. J. He, T. F. Antonios, G. A. MacGregor, and G. R. Sutherland, Regional left ventricular deformation and geometry analysis provides insights in myocardial remodelling in mild to moderate hypertension. *European Heart J. Cardiovascular Imaging* **9** (2008), No. 4, 501–508.
2. R. Burattini and G. Gnudi, Computer identification of models for the arterial tree input impedance: comparison between two new simple models and first experimental results. *Medical Biological Engrg. Computing* **20** (1982), No. 2, 134–144.
3. P. A. Cain, R. Ahl, E. Hedström, M. Ugander, A. Allansdotter-Johnsson, P. Friberg, and H. Arheden, Age and gender specific normal values of left ventricular mass, volume and function for gradient echo magnetic resonance imaging: a cross sectional study. *BMC Medical Imaging* **9** (2009), No. 1. DOI: 10.1186/1471-2342-9-2.
4. A. M. Gordon, E. Homsher, and M. Regnier, Regulation of contraction in striated muscle. *Physiological Reviews* **80** (2000), No. 2, 853–924.
5. J. M. Guccione, A. D. McCulloch, and L. K. Waldman, Passive material properties of intact ventricular myocardium determined from a cylindrical model. *J. Biomechanical Engrg.* **113** (1991), No. 1, 42–55.
6. M. F. Haney, G. Johansson, S. Häggmark, and B. Biber, Method of preload reduction during LVPVR analysis of systolic function airway pressure elevation and vena cava occlusion. *Anesthesiology* **97** (2002), No. 2, 436–446.
7. P. Helm, M. F. Beg, M. I. Miller, and R. L. Winslow, Measuring and mapping cardiac fiber and laminar architecture using diffusion tensor MR imaging. *Annals New York Academy Sci.* **1047** (2005), 296–307.
8. R. B. Hinton and K. E. Yutzey, Heart valve structure and function in development and disease. *Annual Review Physiology* **73** (2011), 29–46.
9. I. Katili, A. Hamdouni, O. Millet, J. I. Rastandi, and I. J. Maknun, A comparative study of stress recovery method and error estimation of plate bending problem using DKMQ element. *Modern Mechanical Engrg.* **2** (2012), 47–55.
10. N. Kawel, B. T. Evrim, J. J. Carr, J. Eng, A. S. Gomes, W. G. Hundley, C. Johnson, S. C. Masri, M. R. Prince, R. J. van der Geest, et al., Normal left ventricular myocardial thickness for middle-aged and older subjects with steady-state free precession cardiac magnetic resonance. *Circulation: Cardiovascular Imaging* **5** (2012), No. 4, 500–508.
11. R. H. Keldermann, M. P. Nash, H. Gelderblom, V. Y. Wang, and A. V. Panfilov, Electromechanical wavebreak in a model of the human left ventricle. *Amer. J. Physiol. Heart Circ. Physiol.* **299** (2010), No. 1, H134–H143.
12. L. Liqi, Y. Shigematsu, M. Hamada, and K. Hiwada, Relative wall thickness is an independent predictor of left ventricular systolic and diastolic dysfunctions in essential hypertension. *Hypertension Research* **24** (2001), No. 5, 493–499.
13. J. F. Marko and E. D. Siggia, Stretching DNA. *Macromolecules* **28** (1995), No. 26, 8759–8770.

14. S. W. Patterson, H. Piper, and E. H. Starling, The regulation of the heart beat. *J. Physiology* **48** (1914), No. 6, 465–513.
15. S. W. Patterson and E. H. Starling, On the mechanical factors which determine the output of the ventricles. *J. Physiology* **48** (1914), No. 5, 357.
16. T. Powell, S. Matsuoka, N. Sarai, and A. Noma, Intracellular Ca^{2+} dynamics and sarcomere length in single ventricular myocytes. *Cell Calcium* **35** (2004), No. 6, 535–542.
17. S. F. Pravdin, V. I. Berdyshev, A. V. Panfilov, L. B. Katsnelson, O. Solovyova, and V. S. Markhasin, Mathematical model of the anatomy and fibre orientation field of the left ventricle of the heart. *Biomedical Engrg. Online* **12** (2013), 54.
18. P. P. Sengupta, A. J. Tajik, K. Chandrasekaran, and B. K. Khandheria, Twist mechanics of the left ventricle. *JACC: Cardiovascular Imaging* **1** (2008), No. 3, 366–376.
19. D. D. Streeter and W. T. Hanna, Engineering mechanics for successive states in canine left ventricular myocardium. II. Fiber angle and sarcomere length. *Circ. Res.* **33** (1973), No. 6, 656–664.
20. D. D. Streeter, H. M. Spotnitz, D. P. Patel, J. Ross, and E. H. Sonnenblick, Fiber orientation in the canine left ventricle during diastole and systole. *Circ. Res.* **24** (1969), No. 3, 339–347.
21. F. A. Syomin, A simple kinetic model of myocardium contraction: Calcium-mechanics coupling. *Biophysics* **59** (2014), No. 5, 772–779.
22. F. A. Syomin and A. K. Tsaturyan, A simple kinetic model of contraction of striated muscle: Full activation at full filament overlap in sarcomeres. *Biophysics* **57** (2012), No. 5, 651–657.
23. F. A. Syomin and A. K. Tsaturyan, A simple model of pumping function of the left ventricle of the heart. *Doklady Biochemistry Biophysics* **462** (2015), No. 1, 158–162.
24. F. A. Syomin, M. V. Zberia, N. A. Koubassova, and A. K. Tsaturyan, Mathematical modelling of the dependence of the performance of the left ventricle of the heart on preload and afterload. *Biophysics* **60** (2015), No. 6, 983–987.
25. I. Teh, D. McClymont, R. A. Burton, M. L. Maguire, H. J. Whittington, C. A. Lygate, P. Kohl, and J. E. Schneider, Resolving fine cardiac structures in rats with high-resolution diffusion tensor imaging. *Scientific Reports* **6** (2016).
26. N. A. Trayanova, Whole-heart modelling: applications to cardiac electrophysiology and electromechanics. *Circ. Res.* **108** (2011), No. 1, 113–128.
27. W. Yu, S. Li, G. Chan, S. Ha, S. J. Wong, and Y. Cheung, Transmural strain and rotation gradient in survivors of childhood cancers. *European Heart J. Cardiovascular Imaging* **14** (2012), No. 2, 175–182.